IEEE Open Journal of Vehicular Technology

Received 22 September 2024; accepted 3 November 2024. Date of publication 7 November 2024;
date of current version 28 November 2024. The review of this article was coordinated by Editor Xianming Qing.

Digital Object Identifier 10.1109/OJVT.2024.3494040

Analysis of Performance and Radiation Regulation Compliance for a Small Sub-Array Based Ka Band Antenna

APARNA P. T. ADITHYABABU [1,2], STEFANO CAIZZONE [1,3] (Member, IEEE), AND RAMON MARTINEZ RODRÍGUEZ-OSORIO [4]

[1]Institute of Communications and Navigation, German Aerospace Center (DLR), 82234 Wessling, Germany
[2]Universidad Politécnica de Madrid (UPM), 28040 Madrid, Spain
[3]Department of Electrical Engineering, Technical University of Munich, 80333 München, Germany
[4]Information Processing and Telecommunications Center (IPTC), Universidad Politécnica de Madrid (UPM), 28040 Madrid, Spain

CORRESPONDING AUTHOR: APARNA P. T. ADITHYABABU (e-mail: aparna.parakkalthachappillyadithyababu@dlr.de).

ABSTRACT The integration of non-terrestrial networks (NTN) and terrestrial networks, driven by the developments in 5G, 5G-advanced, and 6G, have resulted in an abundance of new and unique application scenarios for exploiting existing and upcoming satellite networks. With an increasing number of available satellites, there is a growing demand for user terminals to support NTN services, particularly for earth stations on mobile platforms (ESOMP). In order to allow usability of these user terminals on ESOMPs, low cost, small, and power-efficient antennas need to be developed. Moreover, regulatory issues must be taken into account, in order for the new terminals to be capable to interoperate and not interfere with existing systems. This paper investigates the radiation performance of small Ka band satcom antennas as well as their compliance with current European Telecommunications Standards Institute (ETSI) radiation regulations.

INDEX TERMS Array synthesis, ETSI, Ka band, NTN, radiation regulations, sub-array, user terminals.

I. INTRODUCTION

The integration of non-terrestrial networks (NTN) with the terrestrial networks (TN) aims to provide service continuity, ubiquity, and scalability to the 5th generation (5G) cellular networks [1]. This indicates the possibility to connect the unconnected population, provide services to the underserved areas, and expand the current connectivity services offered by 5G. NTNs can be space-borne using the satellites in low-Earth orbit (LEO), medium-Earth orbit (MEO), or geostationary Earth orbit (GEO), or air-borne using unmanned aerial vehicles (UAV) or high-altitude platform systems (HAPS) [2]. While the existing standards discuss the integration at service level, where TN and NTN remain independent components, 5G advanced and 6G propose fully and seamlessly integrated TN-NTN architecture [3]. Furthermore, the unceasing demand for worldwide connectivity calls for a three-dimensional (3D: ground, air, and space) wireless communication infrastructure for TN-NTN integration [4].

The aforementioned rising connectivity demand has given rise to a plethora of possible applications wanting to leverage the existing and upcoming NTN systems, including connectivity for public safety, defence, aeronautics, automotive, maritime, railway, holographics, and Internet-of-things [3]. The current development in NTN space segments will only benefit these applications if there is a concurrent development in the associated user terminals to access the services. The end user terminals can be classified according to the number of users they have to serve and the performance they need to achieve. For big platforms (like trains/aircraft) or for stationary applications, users require best performance and can afford terminals with large SWaP-C (size, weight, power consumption, and cost). For smaller platforms (such as cars, electrical vertical take off and landing vehicles (eVTOLs) and UAVs), low SWaP-C and lower performance are expected and tolerable due to the small number of users sharing the terminal throughput. To compensate for the communication channel losses and continuously track the satellites, these user

terminals' antennas must have highly directional and steerable beams. Thus, in addition to the complex technology needed at the user terminal to provide the necessary features for connectivity, low-cost, small, and power-efficient terminal antennas are necessary for a better market reach to ensure global connectivity. This paper aims therefore at filling the analysis gap for terminal antennas with low SWaP-C, by focusing on two major aspects: the usability of antennas (phased array antennas in particular) with small footprints and the corresponding achievable performance, as well as the limitations possibly arising from using sub-array-based architectures, needed for price minimization.

Furthermore, it is crucial to ensure coexistence and optimal radio frequency spectrum usage in these expanding numbers of communication networks. To achieve these goals, standardization organizations such as the European Telecommunication Standard Institute (ETSI) and the International Telecommunication Union (ITU) propose a variety of radiation regulations for earth stations operating at various frequencies. These regulations aid in the reduction of terminal radiation emission and interference to neighbouring communication networks, as well as the protection of intended messages from interference from terrestrial and other satellite services. A study on a few chosen regulations from these organizations was conducted in [5], which states that ITU primarily provides an international reference to assist interference studies, while ETSI give patterns that serve as regulatory limits. The study also adds that depending on the application scenario and governing entity, some policies might be more restrictive than the others. In any case, analysis on the adherence to these standards is crucial to ensure that the user terminals can be operated without interfering with surrounding communication networks or receiving interference from other networks.

In this paper, we will analyze the radiation compliance based on existing regulations [6], [7] and identify eventually the limitations and way outs. The compliance for the class of antenna arrays we will analyze is problematic on one hand due to the small aperture, leading to low directivity and broader beam widths in their patterns. Despite the small size, a medium number of antennas and RF channels are still needed in phased arrays, elevating the SWaP-C factor. Therefore, multiple suboptimal solutions such as clustered, thinned, and sparse arrays [8] are available to minimize the number of channels in the phased arrays under analysis. For example, in this study, a sub-array-based (clustering) strategy will be taken into consideration. The use of cost-minimizing techniques such as sub-array based architectures, can only pose additional challenges to the optimal pattern generation of such antennas. Therefore, multiple architectures with different degrees of clustering will be compared to a fully populated array architecture of same size to assess performance as well as regulatory compliance, using the Ka band downlink (20 GHz) scenario as an example.

This paper is organized as follows: Section II discusses the components required for the analysis: arrays subjected to analysis, ETSI radiation regulation, and the array synthesis techniques used. Section III discusses the obtained synthesized patterns and observations. Finally, the conclusions are drawn in Section IV.

TABLE 1. Assumptions for Link Budget Analysis

Parameters	Values
User Terminal	
Antenna Efficiency	70%
Cosine roll-off	1.2
LNA Noise Figure	2 dB
Antenna Noise temperature	50 K
Satellite	
EIRP	43.1 dBW
Channel Bandwidth	100 MHz
Altitude	630 km

II. METHODOLOGY

This paper focuses on an antenna array with a very small aperture size ($\approx$6 cm) that could potentially be used in user terminals on platforms with limited installation area, such as drones or eVTOLs. This chosen dimension would provide a footprint comparable to one of the smallest commercially available UAV terminals, PLANET 9770 UAV-L [9], which has an antenna of diameter 8 cm at L band offering a throughput of 88Kbps using the Iridium Certus^{TM} 100 satellite service. Using such a compact footprint, the following analysis will determine whether we can obtain a higher throughput, utilizing a Ka band antenna.

A. LINK BUDGET ANALYSIS

According to the link budget analysis performed in [2], as the aperture size decreases, so does the attainable throughput. In comparison to the satcom user terminals on commercial aircrafts, which can go up to 106 cm in dimension [10], the size dealt with here is rather small and will result in significantly lesser throughput. However, as compared to commercial aircrafts where the throughput must be shared among a large number of passengers, the number of users in drones or eVTOLs (approximately less than 5 users) are far lower. As a result, in such size-constrained applications, a smaller antenna could still provide good service levels, particularly with the utilization of upcoming LEO satellite constellations [10].Employing the method in [11], a simple link budget analysis (assuming clear sky conditions) was performed with the mentioned aperture size of 6 cm to assess the achievable performance using LEO (Amazon Kuiper taken as reference [12]) link. Utilizing the simplified assumptions in Table 1, a downlink carrier-to-noise ratio (C/N) of $\approx$15 dB was obtained at the user terminal broadside (with $\approx$21.4 dBic antenna gain). Considering 99.9% link availability, a link margin of 6 dB (computed according to [13])) was calculated at broadside to account for additional losses owing to external

TABLE 2. Results of Link Budget Analysis

Parameters	Broadside	Scanning @ 60°
C/N [dB]	≈ 9	≈ 0
SE [bps/Hz]	2.2	0.9
MODCOD	8-PSK 3/4	QPSK 1/2
Throughput [Mbps]	11	4.5

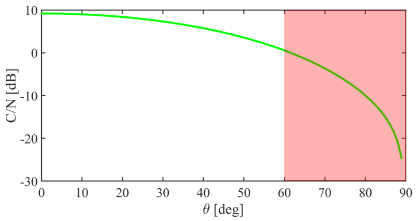

FIGURE 1. Downlink C/N according to the varying scan angle, where C/N < 0 dB is highlighted in red.

factors such as rain fading for the considered link. Thus, a final C/N value of ≈9 dB at broadside was predicted for the terminal under investigation. According to the spectral efficiency (SE) and MODCODs (modulation and coding) offered by DVB S2 or DVB S2X modems [14], [15], this would enable to close the link and have a throughput of around 12 Mbps (as shown in Table 2), in a 5 MHz carrier bandwidth. Hence, this demonstrates that we can achieve significantly higher throughput than employing the previously indicated L band antenna (limited also by the bandwidth availability). For simplicity, we will consider the lower limit for successful connection with satellite to be a C/N of 0 dB and neglect any further reliance on the channel characteristics and modem types. According to the calculations, this limit is obtained at a beam scanning angle of 60° (as shown in Fig. 1), with a corresponding antenna gain of about 17.8 dBic. Link budget results and the possible throughput at this maximum scan angle is also summarized in Table 2.

According to the above calculations, an antenna gain of 17.8 dB or above is considered satisfactory performance at 60° scanning. To distinguish between antennas with tolerable and inadequate performance, further thresholds are defined. DVB S2X supports very low C/N MODCODs which operate at C/N as low as −10 dB [14]. Hence, in order to maintain at least 1 Mbps user throughput (spectral efficiency of at least 0.2 bps/Hz) at 60°, a 6 dB reduction in antenna gain is still deemed tolerable. Antenna performance below this threshold is considered inadequate for satcom applications in this paper.

B. ARRAYS SUBJECTED TO ANALYSIS

To perform a comparative analysis on the obtainable radiation performance and ETSI regulation compliance of the antenna array with the previously mentioned dimension, a rectangular aperture was chosen, with all elements organized in a rectangular lattice. The total radiated field of the planar array was

TABLE 3. Details on Analyzed Arrays

Array	Nx	Ny	dx	dy	≈ Dimension [cm]
A1	8	8	0.5λ	0.5λ	6 × 6
A2	8	4	0.5λ	λ	6 × 6
A3	4	4	λ	λ	6 × 6

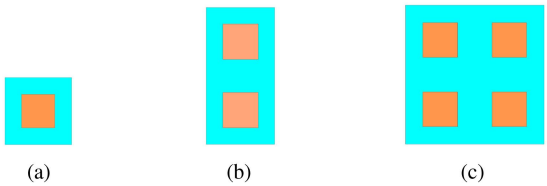

FIGURE 2. Element/cluster of array (a) A1, (b) A2 [16], and (c) A3.

then calculated in a $\{\theta, \phi\}$ angle grid space as,

$$F_{\theta,\phi} = \sum_{n=1}^{N} E_{n\theta,\phi} w_n e^{jk(x_n \sin\theta\cos\phi + y_n \sin\theta\sin\phi + z_n\cos\theta)}, \quad (1)$$

where n denotes the n^{th} element (cluster in case of clustered arrays), N is the total number of elements/clusters, $E_{n\theta,\phi}$ is the single element/cluster pattern extracted from respective simulation models (Ansys HFSS), w_n is the complex excitation, (x_n, y_n, z_n) is the position vector of the body centre of the elements/clusters, k is the wave number $2\pi/\lambda$, and λ is the wavelength. Array synthesis was performed on three distinct arrays A1, A2, and A3 with different clustering levels, details of which are listed in Table 3.

Array A1 is made up of 64 rectangular patch elements (each of dimension 0.5λ × 0.5λ) separated by 0.5λ spacing in both x and y axis. This array contains no element clustering and represents the worst SWaP-C case in terms of cost and power consumption, but at the same time represents the reference architecture, capable of achieving maximum performance due to the maximum number of degrees of freedom and optimal placement of the elements in the grid. Clustering of two elements was performed along one of the dimensions (y axis) in array A2, resulting in 32 sub-arrays (each sub-array with dimension 0.5λ × λ consisting of two patch antenna elements), with their body centre separated by 0.5λ and λ spacing in x and y axis, respectively. This strategy based on sub-arrays (clustering) results in a common control unit to supply complex excitations to all the elements in a sub-array. As a result, this approach halves the number of RF channels and therefore the amount of beam forming chips needed, thereby reducing power consumption and cost in comparison to array A1, which has 64 control units. A higher level of clustering was considered in array A3, where 4 elements were clustered to form the sub-array. This four-element sub-array (each of dimension λ × λ) was then positioned in array with body centre spacing λ in both x and y direction. Fig. 2 depicts the building blocks and Fig. 3 shows the arrays A1, A2, and A3 with body centre of the building blocks depicted by black circle markers.

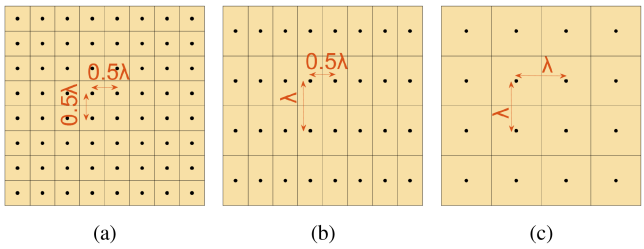

FIGURE 3. Array (a) A1, (b) A2, and (c) A3.

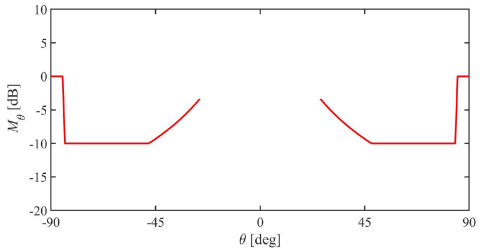

FIGURE 4. 2D Mask M_θ for broadside radiation.

The elements/clusters were arranged in a rectangular lattice to form a rectangular aperture, resulting in the same aperture dimension for all three arrays studied. Though several (better performing) lattices can be used, this lattice was chosen for simplicity and to serve as a reference, i.e. to ensure that the analysis is performed on canonical geometries and is not biased by specific lattice choices. Thus, array A1 was utilized as a reference to establish the maximum achievable radiation performance and ETSI regulation compliance in such a small dimensional antenna array. Furthermore, in this study, array A1 also serves as a reference for clustered arrays in terms of SWaP-C, radiation performance, and radiation regulation compliance. For example, consider employing a Ka band Rx beam former IC such as AWMF-0197 [17] for the three arrays, where each IC can support four dual polarized radiating elements, array A1 would consequently need a total of 16 ICs, whereas arrays A2 and A3 would only need 8 and 4 ICs, respectively. Since beam forming chips have a significant impact on the costs of the terminals, the clustering method will result in significant cost and power consumption reductions for increasing degree of clustering. However, the performance and radiation regulation compliance of these arrays is expected to worsen and must be investigated as shown in the following sections.

For the analysis, the directivity of each of the co-polarized components of the array was calculated as [18]

$$D_{\theta,\phi} = 4\pi \frac{U_{\theta,\phi}}{\int_0^{2\pi}\int_0^{\pi} U_{tot\theta,\phi} \sin\theta d\theta d\phi}, \tag{2}$$

where $U_{tot\theta\phi}$ is the total radiation intensity and $U_{\theta,\phi}$ is the radiation intensity corresponding to one of the co-polarized field components. Since no losses were considered, the directivity (in logarithmic scale) was utilized as an input for the analysis in this study. Mutual coupling and edge effects were not considered in this calculation.

C. ETSI RADIATION REGULATION

No specific standardizations are proposed till date for the new and prospective satcom applications using very small user platforms. An existing standard that is close to the scenario is therefore used as a side lobe control measure. In [6] and [7], ETSI provides the receive antenna off-axis gain pattern specifications for a Ka band ESOMP antenna, operating with GSO and NGSO networks, respectively. This states that the maximum antenna gain of each of the co-polarized components in any direction φ from the antenna main beam axis shall not exceed the following limits:

$$\text{Gain [dBi]} = \begin{cases} 32 - 25\log\varphi, & \text{for } \varphi_{\min} \le \varphi < 48^\circ \\ -10, & \text{for } 48^\circ \le \varphi \le 85^\circ \\ 0, & \text{for } 85^\circ \le \varphi \le 180^\circ, \end{cases} \tag{3}$$

where $\varphi_{\min}$ is 1° or $100\lambda/D$ degrees, whichever is greater for $D/\lambda \ge 50$. For $D/\lambda < 50$, $\varphi_{\min}$ is taken as 2° or $114(D/\lambda)^{-1.09}$ degrees, whichever is greater. The nominal diameter of the antenna is taken as D and the wavelength of operation is taken as λ, for the computation. It is worth noting that ETSI specifies the limits for the side lobe gain but not the maximum allowed gain (main lobe gain) for the receiving antenna.

In this paper, the ETSI pattern given by (3) will be referred to as ETSI mask (M). Since the mask varies depending on the operation frequency and antenna aperture dimensions, the exact dimension and operation frequency of the arrays under investigation were used to generate the mask. The obtained pattern is plotted in Fig. 4 along θ angles for $\phi = \phi_0$, for broadside ($\theta_0 = 0^\circ, \phi_0 = 0^\circ$) radiation case.

Rather than considering a 2D mask, a 3D mask across $\{\theta, \phi\}$ grid is considered in this paper. Therefore, the mask was calculated for each ϕ axis and the obtained pattern is plotted in Fig. 5. As shown later, the compliance to the mask will be calculated such that values above the mask result in non-compliance. Therefore, in order to set a value for the maximum gain in the area $-\varphi_{\min} < \varphi < \varphi_{\min}$ that will not alter compliance, a value of 32 dB (clearly higher than the attainable gain of an array of 6×6 cm^2) will be used. It should be noted that the maximum dimension along each ϕ axis is not the same for rectangular apertures. As a result, the $\varphi_{\min}$ values in (3) for each ϕ axis would be different resulting in patterns derived in Fig. 5. The mask patterns were then used to analyze the arrays A1, A2, and A3's compliance with ETSI radiation regulations. To help readers understand the non-compliance level, the color scale in Fig. 5 is set similarly to the directivity patterns in the following sections.

D. COMPLIANCE ANALYSIS

ETSI regulations require compliance for each of the co-polarized components of the antenna. However, for the sake of simplicity and relying on the symmetry of the structure, only one of the co-polarized components (left hand circular

TABLE 4. Obtained Performance and Non-Compliance Level for Uniform Illumination

(θ_0, ϕ_0) [deg]	D_m* [dB]			NC (L1, L2, L3)[%]		
	A1	A2	A3	A1	A2	A3
(0, 0)	23.2	22.9	23.2	(11.4, 0, 0)	(12.9, 0, 0)	(11.2, 0, 0)
(60, 0)	18.7	18.8	4.2	(16, 7.9, 0)	(16.7, 6.3, 0)	(11, 8.6, 10.6)
(60, 45)	19.5	14.2	9.3	(11.4, 1.5, 0)	(17, 4.3, 1.7)	(22.2, 12.1, 1.4)
(60, 90)	18.9	5.8	4.2	(16.1, 8.1, 0)	(11.2, 8.7, 10.5)	(11.1, 8.7, 10.6)

*D_m corresponds to the maximum total directivity of the array at θ_0, ϕ_0.

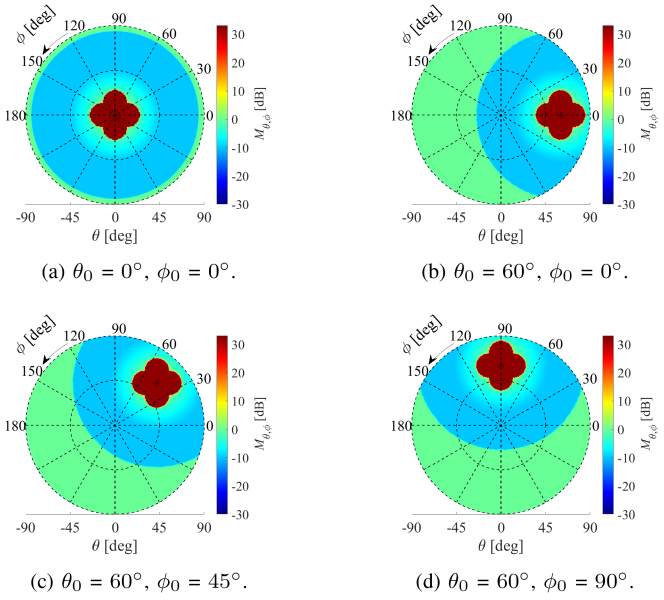

(a) $\theta_0 = 0°$, $\phi_0 = 0°$. (b) $\theta_0 = 60°$, $\phi_0 = 0°$.

(c) $\theta_0 = 60°$, $\phi_0 = 45°$. (d) $\theta_0 = 60°$, $\phi_0 = 90°$.

FIGURE 5. 3D ETSI Mask $M_{\theta,\phi}$ for various steering directions.

polarization: LHCP) of the array was considered in this study. At first, the formulations mentioned in (1-2) were utilized to obtain the LHCP directivity ($D_{\theta,\phi}$) of the three arrays by applying uniform amplitude excitations to all the elements/clusters ($\alpha_n = 1$) and phase excitations (β_n) according to the steering directions (θ_0, ϕ_0). The resulting patterns are plotted in Fig. 6. Taking into account the symmetric lattice layout in the three investigated arrays, only four steering cases ((0°, 0°), (60°, 0°), (60°, 45°), (60°, 90°)) were examined.

To perform the compliance analysis, the ETSI mask ($M_{\theta,\phi}$) was determined in the same θ, ϕ grid space as that of directivity. The grid space was distributed with 1° spacing along θ (−90° to 90°) and ϕ (0° to 360°), resulting in 181 × 361 grid points. Simple matrix subtraction ($D_{\theta,\phi}$ - $M_{\theta,\phi}$) can then be used to check the compliance by determining the difference (error) between these two patterns. The difference patterns were found by subtracting the ETSI mask in Fig. 5 from the directivity in Fig. 6 and are plotted in Fig. 7. The compliant points ($D \leq M$) are ignored in the difference patterns.

Furthermore, as a non-compliance (NC) level measure, 3 levels (L1, L2, and L3) of non-compliance were considered to differentiate the array's performance. The low NC level L1 considers the percentage of non-compliant ($D > M$) points with values less than 10 dB, medium NC level L2 considers values ranging from 10 to 20 dB, and high NC level L3 for values greater than 20 dB. The obtained results for uniformly illuminated arrays A1, A2, and A3 are shown in Table 4. In order to compare the performance of the arrays with varied clustering levels, the maximum total directivity (D_m) at the steering direction (θ_0, ϕ_0) was computed. The values of D_m are color coded based on the threshold defined earlier in Section II-A: green for array gain equal to or above 17.8 dB limit, yellow for tolerable reduction upto −6 dB, and orange as inadequate performance for all other low gain values.

As indicated by directivity values in Table 4, in every scenario investigated, Array A1 performed extremely well matching the previous link budget predictions, proving that small antennas of this kind can be used for satcom applications. Array A2 performs similar to A1 while steering along the $\phi = 0°$ axis. This is due to the fact that the spacing of elements along x ($\phi = 0°$) axis is the same ($\lambda/2$) for both the arrays. When the inter element separation is sufficiently large to allow in-phase addition of radiating fields in more than one direction, the grating lobe appears. Hence, due to the usage of sub-arrays, the spacing of the body centre along the y axis in array A2 is λ, giving rise to grating lobes as expected. Array A3 shows grating lobe in almost all steering directions due to the spacing of λ in both x and y axis. This difference in the directivity patterns can be seen from Fig. 6(h) and (i) where array A2 has a second maxima in addition to the one in the intended direction, and array A3 exhibits three additional maxima. The influence of such grating lobes dominates in array A3 in all cases except the broadside steering case, as indicated by a severe fall in main lobe gain (highlighted in orange in Table 4), making it impossible to close the link at the earlier predicted FoV 60°. Furthermore, it is clear from inspecting the difference patterns in Fig. 7 and Table 4 that non-compliance levels rise along with clustering levels, particularly in high NC level, L3.

E. OPTIMIZATION: GENETIC ALGORITHM

According to the above results, compliance with ETSI regulations is particularly complicated in the context of uniform amplitude excitation. Therefore, a more sophisticated optimization approach, making use of genetic algorithm (GA) [19] to find tapered excitations of the array elements, was performed, in the quest for improved FoV and compliance with ETSI

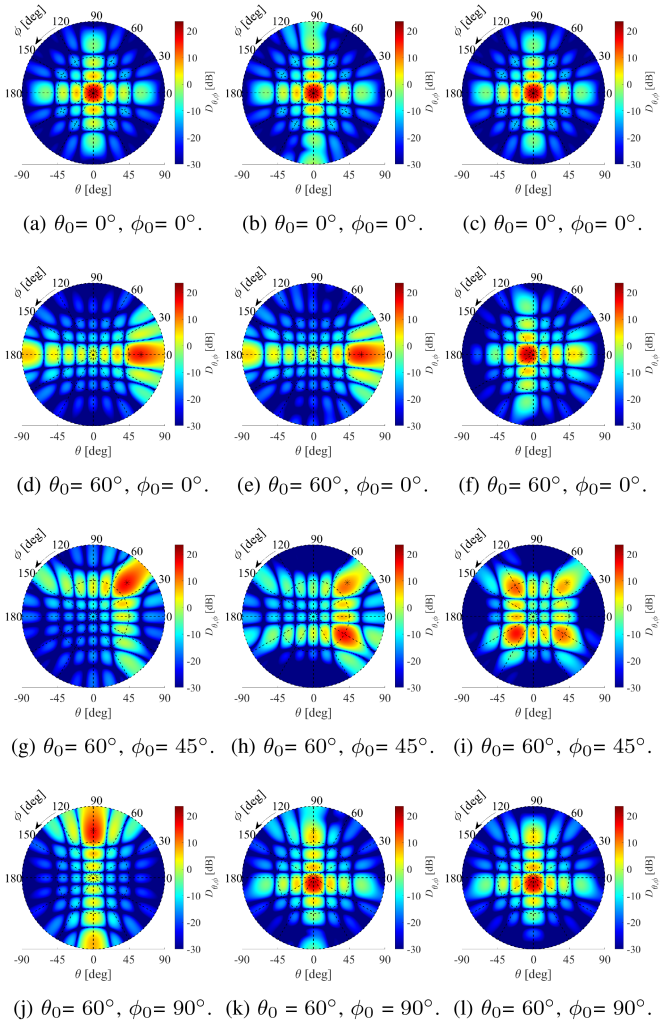

(a) θ_0= 0°, ϕ_0= 0°. (b) θ_0= 0°, ϕ_0= 0°. (c) θ_0= 0°, ϕ_0= 0°.

(d) θ_0= 60°, ϕ_0= 0°. (e) θ_0= 60°, ϕ_0= 0°. (f) θ_0= 60°, ϕ_0= 0°.

(g) θ_0= 60°, ϕ_0= 45°. (h) θ_0= 60°, ϕ_0= 45°. (i) θ_0= 60°, ϕ_0= 45°.

(j) θ_0= 60°, ϕ_0= 90°. (k) θ_0 = 60°, ϕ_0 = 90°. (l) θ_0= 60°, ϕ_0= 90°.

FIGURE 6. Optimized pattern $D_{\theta,\phi}$ using uniform amplitude excitations for A1 (left), A2 (middle), and A3 (right).

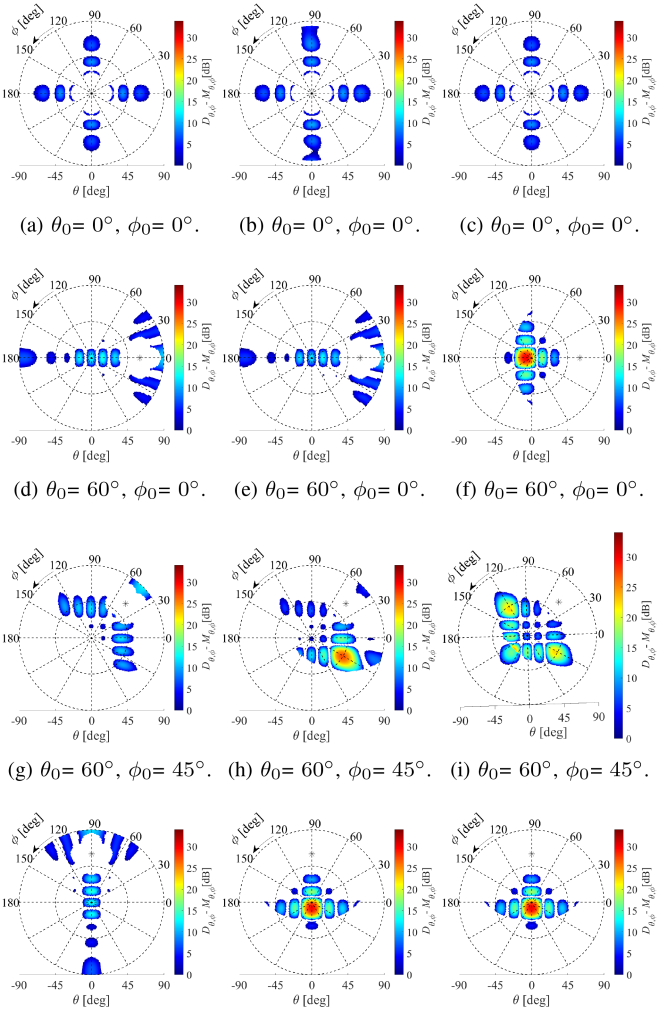

(a) θ_0= 0°, ϕ_0= 0°. (b) θ_0= 0°, ϕ_0= 0°. (c) θ_0= 0°, ϕ_0= 0°.

(d) θ_0= 60°, ϕ_0= 0°. (e) θ_0= 60°, ϕ_0= 0°. (f) θ_0= 60°, ϕ_0= 0°.

(g) θ_0= 60°, ϕ_0= 45°. (h) θ_0= 60°, ϕ_0= 45°. (i) θ_0= 60°, ϕ_0= 45°.

(j) θ_0= 60°, ϕ_0= 90°. (k) θ_0= 60°, ϕ_0= 90°. (l) θ_0= 60°, ϕ_0= 90°.

FIGURE 7. Difference pattern $D_{\theta,\phi}$- $M_{\theta,\phi}$ using uniform amplitude excitations for A1 (left), A2 (middle), and A3 (right).

mask. A population of candidate solutions were randomly generated to initialize the GA. By evaluating an objective function (f), the population was evaluated and made to undergo sorting and selection, followed by reproduction through crossovers and mutation to form the new population [19]. This process was then repeated until the objective ($f = 0$) was met or the maximum number of iterations was reached. The crossover and mutation were performed according to user-specified crossover probability (cp) and mutation probability (mp). Values of 0.7 and 0.5 were chosen in this paper, for cp and mp, respectively. GA was repeated several times using random seeds (s) as the initial population, and the best seed (the one rendering lowest value for the objective function) was chosen as the end outcome of the optimization. The number of iterations was set to 400, and the population size (p) was determined by the number of unknowns/variables (v) to be optimized.

The optimization (performed in MATLAB [20]) was set with the goal of minimizing the objective cost function given below.

$$f = wc_1(D_{req} - D_{cal})^2_{\theta_0,\phi_0} + wc_2C, \tag{4}$$

where

$$C = \frac{\sum_{i=1}^{gp} c(D_i - Mi)^2}{gp_{tot}}$$

$$c = \begin{cases} 1, & \text{for } D_i > M_i \\ 0, & \text{for } D_i \leq M_i, \end{cases} \tag{5}$$

where D_{req} is the desired/required maximum directivity and D_{cal} is the calculated maximum directivity in the steering direction (θ_0, ϕ_0), gp is the number of grid points where the pattern is not compliant, gp_{tot} is the total grid points, and c is the weighting coefficient.

The parameter C is a weighted mean-square-error (MSE) where only non-compliant ($D > M$) points are considered (weighted with value 1) and the compliant points ($D \leq M$) are ignored (weighted with value 0). To prioritize the array

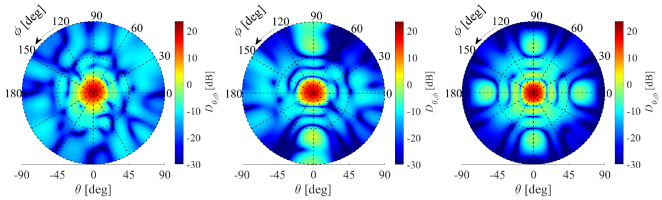

(a) θ_0= 0°, ϕ_0= 0°. (b) θ_0= 0°, ϕ_0= 0°. (c) θ_0= 0°, ϕ_0= 0°.

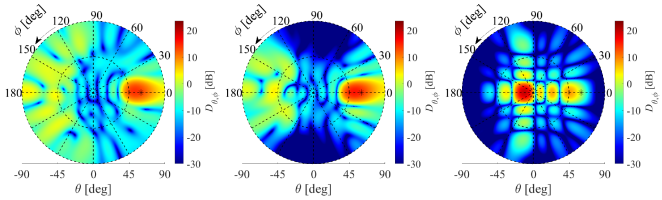

(d) θ_0= 60°, ϕ_0= 0°. (e) θ_0= 60°, ϕ_0= 0°. (f) θ_0= 60°, ϕ_0= 0°.

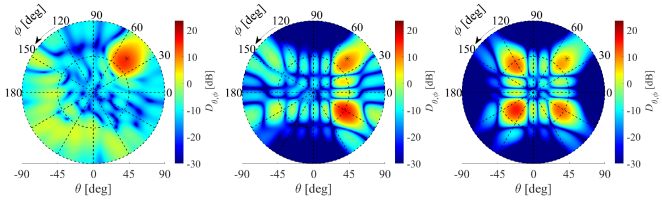

(g) θ_0= 60°, ϕ_0= 45°. (h) θ_0= 60°, ϕ_0= 45°. (i) θ_0= 60°, ϕ_0= 45°.

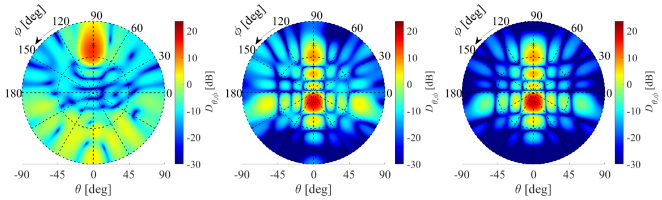

(j) θ_0= 60°, ϕ_0= 90°. (k) θ_0= 60°, ϕ_0= 90°. (l) θ_0= 60°, ϕ_0= 90°.

FIGURE 8. Optimized pattern $D_{\theta,\phi}$ for A1 (left), A2 (middle), and A3 (right).

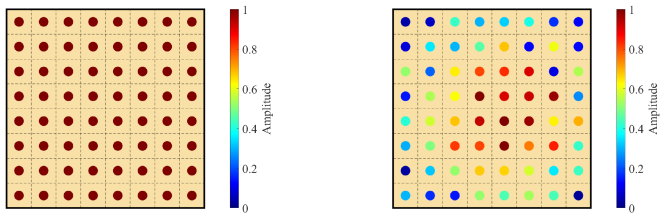

(a) Uniform excitation. (b) Tapered excitation.

FIGURE 9. Amplitude excitations of A1 for steering case $\theta_0 = 0°$, $\phi_0 = 0°$.

synthesis goals, the two terms in (4) were weighted with weighting coefficients wc_1 and wc_2. For instance, wc_1 and wc_2 were taken as 0.1 and 10, respectively, for majority of the analysis cases, except for cases with grating lobes, where they were assumed as 0.2 and 0.8. These parameter values were chosen in such a way that mask compliance (second term in (4)) was prioritized while still attempting to direct the main lobe of radiation in the required direction.

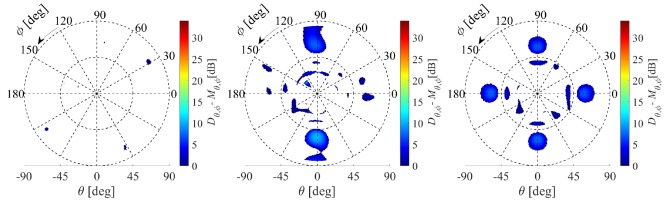

(a) θ_0= 0°, ϕ_0= 0°. (b) θ_0= 0°, ϕ_0= 0°. (c) θ_0= 0°, ϕ_0= 0°.

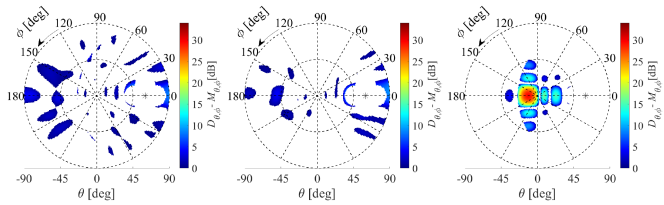

(d) θ_0= 60°, ϕ_0= 0°. (e) θ_0= 60°, ϕ_0= 0°. (f) θ_0= 60°, ϕ_0= 0°.

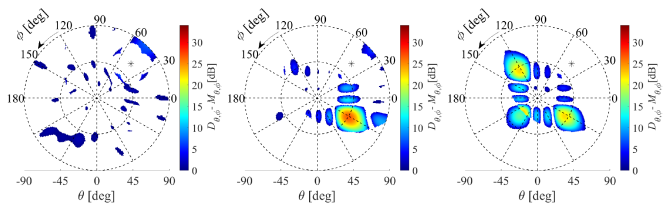

(g) θ_0= 60°, ϕ_0= 45°. (h) θ_0= 60°, ϕ_0= 45°. (i) θ_0= 60°, ϕ_0= 45°.

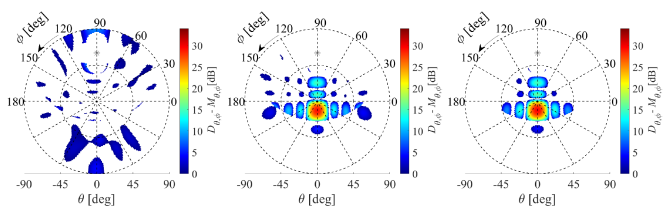

(j) θ_0= 60°, ϕ_0= 90°. (k) θ_0= 60°, ϕ_0= 90°. (l) θ_0= 60°, ϕ_0= 90°.

FIGURE 10. Difference pattern $D_{\theta,\phi}$-$M_{\theta,\phi}$ after optimization for A1 (left), A2 (middle), and A3 (right).

III. ANALYSIS

The GA optimization attempting to create tapered pattern took into account the excitations of all the building blocks. The excitations obtained for one of the analyzed cases are shown in Fig. 9 in comparison to the uniform excitation. It is evident that the GA optimization resulted in a non-uniform distribution, which in turn provided a tapering pattern as in Fig. 8(a) by giving high amplitudes to centre elements and low amplitudes for distant elements in the element distribution in the aperture. Since the obtained excitations vary for each of the optimized steering case, we choose not to incorporate this into the paper ro reduce further complexity. After running the optimization, the obtained LHCP directivity pattern ($D_{\theta,\phi}$), and the difference pattern ($D_{\theta,\phi}$-$M_{\theta,\phi}$) of all cases are plotted in Figs. 8 and 10, respectively. The convergence of the objective function over iterations of the best GA seeds are plotted in Fig. 11. The observed maximum directivity along with the non-compliance level is displayed in Table 5 for all the optimized arrays.

TABLE 5. Obtained Performance and Non-Compliance Level After Optimization

(θ_0, ϕ_0) [deg]	D_m [dB]			NC (L1, L2, L3)[%]		
	A1	A2	A3	A1	A2	A3
(0, 0)	21.3	21.5	22.7	(0.4, 0, 0)	(10.3, 0, 0)	(9.9, 0, 0)
(60, 0)	16.4	17.5	3	(13.7, 0, 0)	(8.9, 0, 0)	(11.1, 10.1, 7)
(60, 45)	17	14	9	(9, 0, 0)	(9.8, 2.3, 1.7)	(15.3, 8.6, 1.6)
(60, 90)	16.5	4.3	3	(15.3, 0, 0)	(15, 10, 6.3)	(11.2, 10.2, 7)

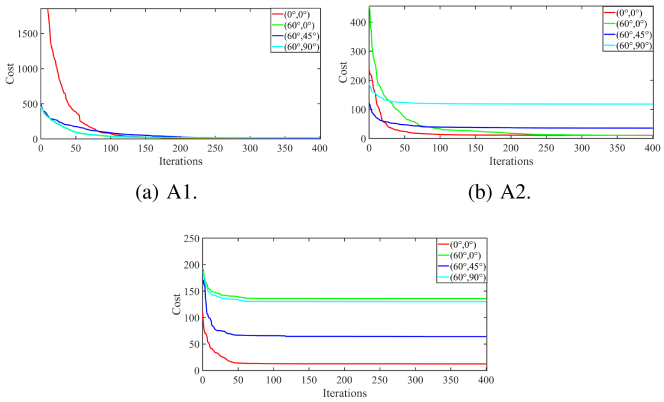

(a) A1. (b) A2.

(c) A3.

FIGURE 11. Convergence curve from the cost function of GA best seeds.

A. OBSERVATIONS

As anticipated, the maximum directivity will slightly reduce as the element excitations distribution changes from uniform to tapered illumination. Ideally, the non-compliance level measure would return a value of 0 if the ETSI mask is completely satisfied. According to the obtained results, this objective was only accomplished for array A1 at broadside. Even with comparable performance, the shaped patterns produced by optimization exhibits better compliance than the uniformly illuminated arrays in almost all cases. Notably, in majority of cases, arrays A1 and A2 significantly reduced non-compliance to 0% in L2 and L3, compared to the results in Table 4.

In Table 5, array A1 exhibits growing non-compliance in L1 as the steering angle increases in any direction. Although array A1 could completely fulfil the ETSI mask at broadside, array A2 (non-compliance mostly around $\phi = 90^\circ$) and A3 (non-compliance along both $\phi = 0^\circ$ and $\phi = 90^\circ$ axes) do not conform to the mask already at broadside. This is related to the concept of sub-array/cluster level excitations (complex excitations considered at cluster's body centre) rather than element level excitations. As the steering angle θ_0 increases along $\phi = 0^\circ$, array A2 shows comparable performance to A1 (due to similar lattice arrangement in $\phi = 0^\circ$ axis), even with fewer control points. Array A3, on the other hand, performed poorly in terms of both performance and compliance, even after optimization, owing mostly to the lower degree of freedom of excitations points, which also gave rise to grating lobes in almost all the examined steering directions.

Based on the aforementioned results and analysis, array with two-element clusters (Domino [16]) appears to be a reasonable trade-off for reducing SWaP-C without compromising too much on the antenna performance. Furthermore, in array A2, performance and the non-compliance level is quite acceptable where the inter-element distance is $\lambda/2$, but unsatisfactory on the other axis. It is thus worthwhile to investigate arrays based on 2-element clusters that exhibit "balanced" intermediate distances by employing exotic lattices.

B. DOMINO ZIGZAG ARRAY

It is clear from the preceding sections that improving directivity in a steering direction and suppressing side lobes or grating lobes cannot be achieved on array A2 by optimizing excitations alone. Instead of the earlier assumed regular lattice arrangement, the 2-element clusters (Dominos) can be arranged either horizontally or vertically in the 6 cm aperture, resulting in a Domino 'zigzag' array. Owing to the wide range of potential lattice arrangements, four distinct trials comprising 7000 possible configurations were evaluated and the lattice design that yields the best outcomes for various steering cases was chosen. Since the lattice arrangement is not symmetric in x-y plane, 9 steering cases (5 additional cases than previous analysis) covering the upper hemisphere of the 3D radiation pattern were considered for optimization. Thus, through repeated iterative process, the lattice arrangement in Fig. 13 was selected which showed the lowest MSE when compared to uniformly illuminated array A1. Subsequently, optimization on the element excitations was performed as mentioned in Section II-E on the zig-zag array to bring down the side lobes. The final optimized directivity and difference patterns and compliance levels are given in Fig. 12 and Table 6, respectively.

It can be observed that the maximum obtainable directivity is almost consistent at 60° scanning along all the investigated ϕ cases unlike regular lattice array A2. The earlier grating lobe occurrence shown by A2 at $\phi = 90^\circ$ is mitigated with the chosen irregular lattice arrangement. This would then result in a consistent FoV for the terminal in all examined steering cases. It is clear that, the Domino Zigzag array achieves 50% less SWaP-C while still performing reasonably well in comparison to a fully populated array of the same dimension.

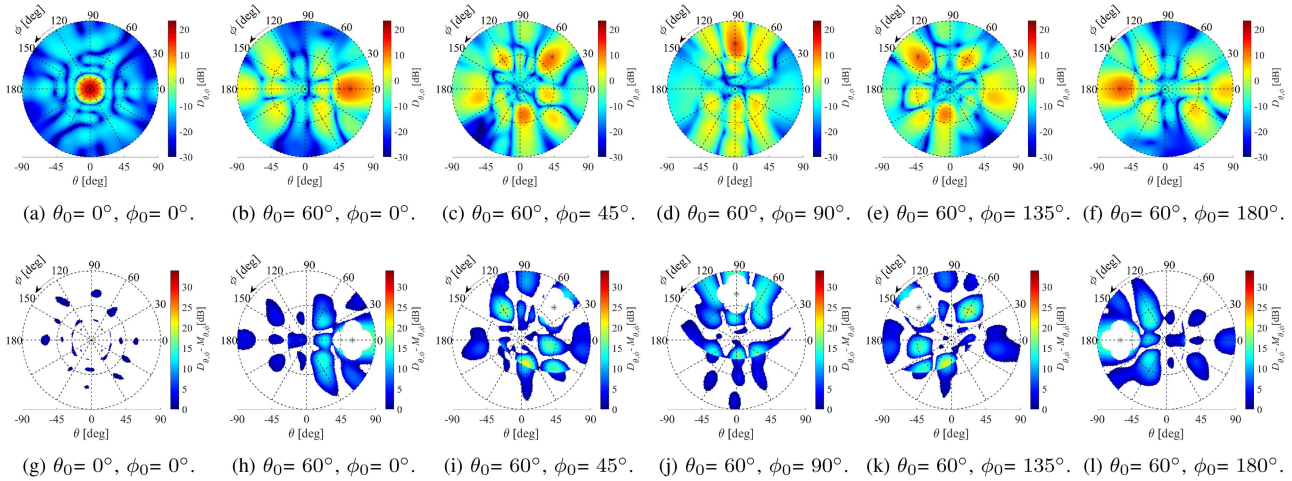

(a) θ_0= 0°, ϕ_0= 0°. (b) θ_0= 60°, ϕ_0= 0°. (c) θ_0= 60°, ϕ_0= 45°. (d) θ_0= 60°, ϕ_0= 90°. (e) θ_0= 60°, ϕ_0= 135°. (f) θ_0= 60°, ϕ_0= 180°.

(g) θ_0= 0°, ϕ_0= 0°. (h) θ_0= 60°, ϕ_0= 0°. (i) θ_0= 60°, ϕ_0= 45°. (j) θ_0= 60°, ϕ_0= 90°. (k) θ_0= 60°, ϕ_0= 135°. (l) θ_0= 60°, ϕ_0= 180°.

FIGURE 12. Optimized pattern $D_{\theta,\phi}$ (top) and difference pattern $D_{\theta,\phi}$-$M_{\theta,\phi}$ (bottom) for Domino zigzag array.

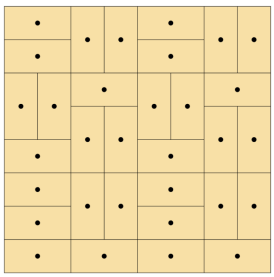

FIGURE 13. Optimized domino zigzag array.

TABLE 6. Optimized Performance and Non-Compliance Level for Domino Zigzag Array

(θ_0, ϕ_0) [deg]	D_m [dB]	NC (L1, L2, L3) [%]
(0, 0)	21.7	(6.5, 0, 0)
(60, 0)	15.3	(37, 6, 0)
(60, 45)	13.5	(34, 7, 0)
(60, 90)	15.2	(33, 9.8, 0)
(60, 135)	13	(31, 7.3, 0)
(60, 180)	14.6	(39, 6.4, 0)
(60, 225)	13	(34, 6.8, 0)
(60, 270)	15	(35, 10, 0)
(60, 315)	13.5	(35, 7, 0)

While the NC levels in Table 6 indicates a few significantly big side lobes that need to be mitigated, it is important to notice that none of the grating lobes in the domino zigzag array are higher than the main lobe in all examined cases and main lobe value always falls in the earlier defined tolerable (yellow) performance range.

IV. CONCLUSION

This paper studied three array antennas with varying clustering levels to lower the SWaP-C of satcom user terminals and evaluated their limits in terms of radiation performance and regulatory compliance. Small arrays have the ability to meet the needs of satcom connectivity, but they also have constraints that was carefully examined. Cost and power consumption of the terminal antennas can be decreased with a higher level of clustering. However, as the clustering level grows, the antenna's performance diminishes as expected from theory. As a result, this article aided in determining a trade-off between radiation performance and SWaP-C reduction by quantifying the influence of small footprints and clustering. Although several constraints were observed, and further optimization is required, this study demonstrates the feasibility of employing compact Ka band antennas on small user platforms, as well as the potential to achieve higher throughput than the commercially available L band antennas. Additionally, irregular lattice arrangement of clusters was also investigated to obtain tolerable antenna performance over wide range of scan angles. Moreover, further research is envisaged to optimize and bring further the obtained results in terms of directivity, side lobe levels and grating lobe mitigation. Further, the analyzed array in this paper can be realized using the manufactured domino elements in [16] and beam former board in [21], at DLR.

REFERENCES

[1] 3rd Generation Partnership Project, "Technical specification group services and system aspects," Study on Using Satellite Access in 5G, Stage 1 (Release 16), 3rd Generation Partnership Project, Sophia Antipolis, France, Tech. Rep. 22.822 V16.0.0, Jun. 2018. [Online]. Available: https://portal.3gpp.org/desktopmodules/Specifications/SpecificationDetails.aspx?specificationId=3372

[2] A. P. T. Adithyababu, F. Boulos, and S. Caizzone, "Analysis of user terminal trade-offs for future satellite communication applications," in *Proc. 27th Ka Broadband Commun. Conf.*, Stresa, Italy, Oct. 2022, pp. 18–21.

[3] A. Vanelli-Coralli, A. Guidotti, T. Foggi, G. Colavolpe, and G. Montorsi, "5G and beyond 5G non-terrestrial networks: Trends and research challenges," in *Proc. 2020 IEEE 3rd 5G World Forum*, 2020, pp. 163–169.

[4] G. Geraci, D. López-Pérez, M. Benzaghta, and S. Chatzinotas, "Integrating terrestrial and non-terrestrial networks: 3D opportunities and challenges," *IEEE Commun. Mag.*, vol. 61, no. 4, pp. 42–48, Apr. 2023.

[5] H. Mazar, "Regulating and standardizing directive antenna patterns to improve coexistence," in *Proc. 2018 Texas Symp. Wireless Microw. Circuits Syst.*, Waco, USA, Apr. 2018, pp. 1–6.
[6] *Satellite Earth Stations and Systems (SES); Harmonised Standard for Earth Stations on Mobile Platforms (ESOMP) Transmitting Towards Satellites in Geostationary Orbit, Operating in the 27,5 GHz to 30,0 GHz Frequency Bands Covering the Essential Requirements of Article 3.2 of the Directive 2014/53/EU*, ETSI Standard EN 303 978 V2.1.2, European Telecommunications Standards Institute: Sophia Antipolis, France, 2016.
[7] *Satellite Earth Stations and Systems (SES); Harmonised Standard for Earth Stations on Mobile Platforms (ESOMP) Transmitting Towards Satellites in Non-Geostationary Orbit, Operating in the 27,5 GHz to 29,1 GHz and 29,5 GHz to 30,0 GHz Frequency Bands Covering the Essential Requirements of Article 3.2 of the Directive 2014/53/EU*, ETSI Standard EN 303 979 V2.1.1, European Telecommunications Standards Institute: Sophia Antipolis, France, 2016.
[8] P. Rocca, G. Oliveri, R. J. Mailloux, and A. Massa, "Unconventional phased array architectures and design methodologies—A review," *Proc. IEEE*, vol. 104, no. 3, pp. 544–560, Mar. 2016.
[9] Planet 9770 UAV-L Terminal Datasheet, Sep. 2023. [Online]. Available: https://store.atmosphere.aero/img/cms/PLANET_9770_UAV-L_Terminal_V1-0.pdf
[10] A. P. T. Adithyababu, F. Boulos, and S. Caizzone, "Avionic satellite communication terminal requirements and technology maturity analysis," *IEEE Aerosp. Electron. Syst. Mag.*, vol. 39, no. 1, pp. 4–17, Jan. 2024.
[11] "Link budget calculations for a satellite link with and electronically steerable antenna terminal," Jun. 2019. Accessed: Nov. 2023. [Online]. Available: https://www.satnow.com/whitepapers/details/15-link-budget-calculations-for-a-satellite-link-with-an-electronically-steerable-antenna-terminal
[12] G. Amendola et al., "Low-earth orbit user segment in the Ku and Ka-band: An overview of antennas and RF front-end technologies," *IEEE Microw. Mag.*, vol. 24, no. 2, pp. 32–48, Feb. 2023.
[13] "Propagation data and prediction methods required for the design of Earth-space telecommunication systems," Recommendation ITU-R P.618-14, Jun. 2023. [Online]. Available: https://www.itu.int/dms_pubrec/itu-r/rec/p/R-REC-P.618-14-202308-I!!PDF-E.pdf
[14] "White paper on the use of DVB-S2X for DTH applications, DSNG & professional services, broadband interactive services and VL-SNR applications," Mar. 2015. [Online]. Available: https://dvb.org/wp-content/uploads/2020/01/a172_dvb-s2x_highlights_-_white_paper.pdf
[15] X. Wang, H. Li, and Q. WU, "Optimizing adaptive coding and modulation for satellite network with ML-based CSI prediction," in *Proc. IEEE Wireless Commun. Netw. Conf.*, 2019, pp. 1–6.
[16] F. Boulos, U. Johannsen, and S. Caizzone, "Customizable phased array antenna based on domino tiles for satcom applications," in *Proc. 2022 IEEE Int. Symp. Phased Array Syst. Technol.*, 2022, pp. 01–05.
[17] "Product overview: K-band quad 4x2 Rx beamformer IC AWMF-0197," Rev. 3, San Diego, CA, USA, Anokiwave, Inc., Oct. 2023. [Online]. Available: https://www.anokiwave.com/products/awmf-0197/index.html
[18] C. A. Balanis, "Fundamental parameters and figures-of-merit of antennas," in *Antenna Theory; Analysis and Design*, 4th ed. Hoboken, NJ, USA: Wiley, 2016.
[19] R. Jain and G. Mani, "Dynamic thinning of antenna array using genetic algorithm," *Prog. Electromagnetics Res. B*, vol. 32, pp. 1–20, Jan. 2011.
[20] "MATLAB R2023a," The MathWorks, Inc., 2023.
[21] F. Boulos, E. O. Addo, S. Caizzone, and U. Johannsen, "A modular, low-cost Ka-band antenna subarray as building block for phased arrays of arbitrary size and shape," in *Proc. 18th Eur. Conf. Antennas Propag.*, 2024, pp. 1–4.

APARNA P. T. ADITHYABABU received the B.Tech. degree in electronics and communication engineering from the Amrita School of Engineering, Kerala, India, in 2017, and the M.Sc. degree in communications engineering from the University of Applied Sciences, Darmstadt, Germany, in 2021. Since 2023, she has been working toward the Ph.D. degree with the Program Communication Technologies and Systems, Universidad Politécnica de Madrid, Spain. As part of DLR-DAAD Research Fellowship Program, she is currently a member of the Antenna Systems Group, Institute of Communications and Navigation of the German Aerospace Center (DLR), where she is working on steerable high-performance antenna systems for global connectivity.

STEFANO CAIZZONE (Member, IEEE) received the M.Sc. degree in telecommunications engineering and the Ph.D. degree in geoinformation from the University of Rome "Tor Vergata", Rome, Italy, in 2009 and 2015, respectively. Since 2010, he has been with the Antenna Group of the German Aerospace Center (DLR), where he has been responsible for the development of innovative miniaturized antennas. Since July 2020, he leads the Antenna Systems Group. His main research interests include small antennas for satellite navigation, controlled radiation pattern antennas for robust satellite navigation and high-performance antenna design for precise satellite navigation, antenna arrays for satellite communication and installed performance analysis.

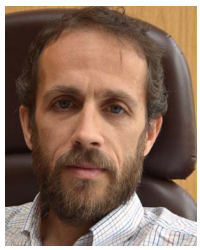

RAMON MARTINEZ RODRÍGUEZ-OSORIO received the Telecommunication Engineering degree and Ph.D. degree in telecommunication engineering from the Universidad Politécnica de Madrid (UPM), Madrid, Spain, in 1999 and 2004, respectively. He is currently Full Professor (Catedrático) with the Telecommunication Engineering School (ETSIT-UPM). Prof. Martínez has held several academic management positions in his career, and since 2021 he is Adjunct Vicerrector for Academic Planning at UPM. In the framework of his research works, he has led and participated in a number of international projects in the area of space technology for small satellites, antennas for inter satellite links, geolocation of interferences and the application of antenna arraying to wireless and space missions. He has led the design of HispaSim, a platform for the design and optimization of satellite links under contract with GMV and Hispasat, and has an active role in technology transfer with industry, being coauthor of five patents. Prof. Martínez has been a Lecturer in SatCom systems since 2004, introducing novel learning methodologies based on project-based learning approach. He has coordinated SatCom and antenna arraying and MIMO courses at Master level since 2006. He also leads the activities in nanosatellite technology with students in ETSIT-UPM. Prof. Martínez was the recipient of the UPM Prize for his Innovative Education Activities in 2011.